HardwareX 16 (2023) e00480

Contents lists available at ScienceDirect

HardwareX

journal homepage: www.elsevier.com/locate/ohx

Hardware article

Multimodal fluorescence microscope with fast adaptive polarimetry

Berta Martínez-Prat, Oriol Arteaga, Francesc Sagués, Jordi Ignés-Mullol *

Universitat de Barcelona and Institute of Nanoscience and Nanotechnology (IN2UB), Martíi Franquès 1, 08028, Barcelona, Spain

ARTICLE INFO

Keywords:
Birefringence
Anisotropy
Optical microscopy
Fluorescence microscopy

ABSTRACT

Polarized light microscopy is a widely used technique to observe specimens that are optically anisotropic, or birefringent. It has a broad applicability in the study of minerals, soft materials such as polymers, complex fluids or liquid crystals, and organic tissues in biology and medicine. Most of these observations are qualitative in nature, as it is not obvious to quantify the spatial distribution of optical anisotropy of specimens. Moreover, existing commercial implementations for quantitative polarimetry are costly and slow in nature, precluding real time observation of dynamical processes. Here, we present a custom-made implementation of an optical microscope for quantitative polarimetry at the cost of a standard scientific polarizing microscope. The instrument allows to extract the local optical axis and birefringence of transparent materials with a frequency of several Hz. The instrument is built using off-the-shelf optomechanical components, which optimizes cost, availability, and modularity. An example of the latter is the fact that we combine the polarimetry measurements with simultaneous fluorescence microscopy, which results in a powerful multimodal instrument with broad potential applications.

* Corresponding author.
E-mail address: jignes@ub.edu (J. Ignés-Mullol).

https://doi.org/10.1016/j.ohx.2023.e00480
Received 3 March 2023; Received in revised form 2 August 2023; Accepted 18 September 2023
Available online 27 September 2023

Specifications table:

Hardware name	Fast adaptive polarimetry and fluorescence microscope
Subject area	• Material science • Physical chemistry • Colloids, liquid crystals, and complex fluids • Biological materials
Hardware type	• Imaging tools • Measuring physical properties and in-lab sensors • Field measurements and sensors • Mechanical engineering and materials science
Hardware characteristics	• Field of view of 700 μm, with 10x objectives and the used cameras • Spatial resolution of 1.2 μm/pixel, with 10x objectives, the used cameras, and no binning • Rate of full polarimetry frame capture of 2.5 Hz
Closest commercial analog	• OpenPolscope. Basic kit to adapt to an existing polarization microscope. Slow performance (several seconds). • Oosight (Hamilton Thorne) and Abrio (Perkin Elmer). More user friendly implementations that assemble into a standard microscope. Costly and slow performance (several seconds). • PolarAIDE (OCTAX). A basic, qualitative implementation. Not for quantitative purposes. • Exicor Microimager (Hinds Instruments). Complete setup based on the OpenPolscope. Good sensitivity but very slow performance (nearly ten seconds). • Birefringent Imaging System (Thorlabs LCC7201B). Standalone setup based on a LC retarder. Also, for improved modularity, Cerna Birefringence Imaging Microscope (Thorlabs). Good sensitivity, but very slow performance (20 s).
Open source license	CC BY-NC-ND
Cost of hardware	8400€ + cost of cameras and software licenses (complete breakdown will be included in the Bill of Materials). Prices up to date in July 2023.
Source file repository	https://doi.org/10.17605/OSF.IO/BDS26

1. Hardware in context

Quantitative polarization microscopy [1–3] is a powerful technique in materials science and biology for the noninvasive characterization of microstructures without the need to use chemical dopants (such as fluorescence probes or stains). The single requirement for its usability is the presence of optical anisotropy, or birefringence, either in the studied materials or in their surroundings. This property is prevalent among soft materials, such as polymers, liquid crystals, colloidal suspensions, and most biofluids and intracellular structures [4]. Moreover, this approach does not require high dosages of irradiation such as in fluorescence microscopy to provide good optical contrast and can take advantage of differential birefringence between neighboring structures, such as in the intracellular environment, to provide the same, or even more information than multiprobe fluorescence microscopy or differential interference contrast microscopy.

The most successful implementation of quantitative polarization microscopy to date is the Open Polscope, invented by Rudolf Oldenbourg [5] around 25 years ago , which has found widespread application in a broad spectrum of fields, from materials science to biomedicine [6–8]. In order to resolve the local birefringence and slow polarization axis (which typically coincides with the alignment direction of fibers or molecules), the Open Polscope acquires and combines several images with different polarization configurations. In this setup, this is achieved through a variable liquid crystal compensator (also called “universal compensator”). This device consists of a thin layer of liquid crystal placed between parallel electrodes, with a slow axis that is aligned along a predetermined direction by means of physicochemical methods that are well-known in the liquid crystal industry. Through application of an electric field, the retardance of this variable compensator can be precisely and reversibly set [9], without the alignment and mechanical issues that may arise when using rotating compensators.

This idea has been implemented by a number of specialized, technically capable laboratories, in particular among the liquid crystal community, and it has resulted in several commercial products. Within the past five years, we can find hundreds of references to “OpenPolscope”, “Polscope” or “LC-Polscope” in the literature. As examples of recent publications in a broad spectrum of fields where these devices are used for quantitative polarization microscopy, we can cite studies within the liquid crystal community [10–14], soft mater studies of in-vitro reconstitutions of cytoskeleton proteins [15,16], intracellular studies [17–19], and advanced functional materials [20] and biomaterials [21]. The measurements performed within this literature are mostly restricted to simple birefringence measurements and slow axis determination, and to quasi-stationary samples. Indeed, commercial realizations are intrinsically slow, requiring several seconds to acquire the images required to resolve the birefringence map. The ability to perform real time measurements (several measurements per second) is restricted to laboratories with the technical capabilities to implement enhanced setups [14], but it would certainly benefit most researchers currently using Polscope-like instruments to have access to a faster and more economical implementation.

When studying soft matter dynamic systems of permanent flowing nature, both the birefringence and velocity fields are essential to fully characterize the process at hand. Velocity measurements are typically performed using particle image velocimetry, a

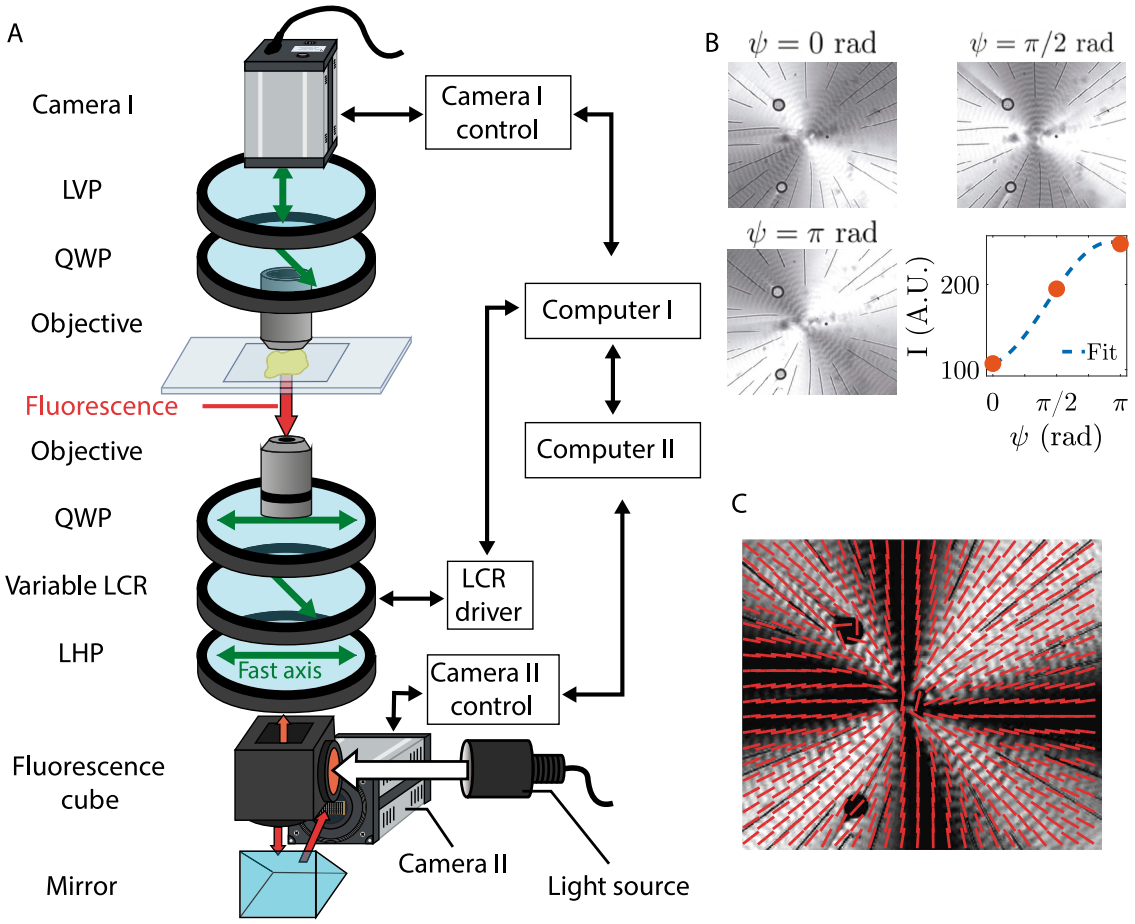

Fig. 1. A. Schematic experimental setup of the fast adaptive polarimeter. Light from a collimated LED source is deflected by the dichroic mirror of a CYT5 fluorescence cube. Then it is linearly polarized by a horizontal polarized (LHP) modulated by a variable Liquid Crystal Retarder whose fast axis is rotated 45° CCW with respect to LHP. The modulated light is focused on the sample by an infinity-corrected objective. An identical objective captures the light past the sample and is modulated by a QWP with fast axis rotated 45° CCW and filtered by a vertical linear polarized (LVP) before being focused to Camera I. In the diagram, green arrows indicate the orientation of the fast axis of birefringent elements. Samples with compatible fluorescent dyes generate an amount of emitted light that is selected by the fluorescence cube before being focused on the high-sensitivity Camera II. The variable LCR and Camera I are controlled by Computer I, which is synchronized with Computer II, which handles acquisition of fluorescence images with Camera II. **B**. Micrographs at different dispositions of the variable LCR and pixel-level fit of Eq. (9) to extract the relevant material parameters. **C**. Result of the polarimetry after fitting all pixels in the acquired images.

video-microscopy technique that compares the local displacement of microparticles that have been seeded in the system. Here, we demonstrate that our modular implementation of a quantitative polarization microscope can be easily extended to provide simultaneous fluorescence microscopy that can be employed, for instance, to visualize seeded fluorescence microparticles, thus obtaining simultaneous but decoupled birefringence and velocity fields. The budget nearly doubles when including the fluorescence module, because of the cost of a fluorescence-grade camera that, nevertheless, could be included in future upgrades of the system.

2. Hardware description

We describe a multimode microscope that combines epi-fluorescence microscopy and quantitative polarimetry so that both techniques can be used independently or simultaneously. The transmitted light from the fluorescence module is employed by the polarimetry module to measure the birefringence and optical axis of the samples. Indeed, the two techniques are optically decoupled, as fluorescence is, in general, insensitive to the state of polarization of incident light. Because of the polarization-active optical elements, the light reaching the fluorescence camera will be less than 25% the amount for a standalone fluorescence module. In our experience, modern fluorescence probes, a mid-range fluorescence camera, and a 1 W LED source yield good signal-to-noise fluorescence images. A voltage-controlled LC retarder allows to obtain images with different superimposed retardances, thus enabling to resolve the local slow axis of a birefringent material and its birefringence if the total retardance is below 160 nm, approximately. For larger retardances, only the local slow axis is obtained. The switching times between the different configurations of the LC retarder are optimized so that a rate of 2 frames per second can be easily achieved. This is in contrast with existing implementations of the LC-Polscope, that require several seconds to obtain a full image.

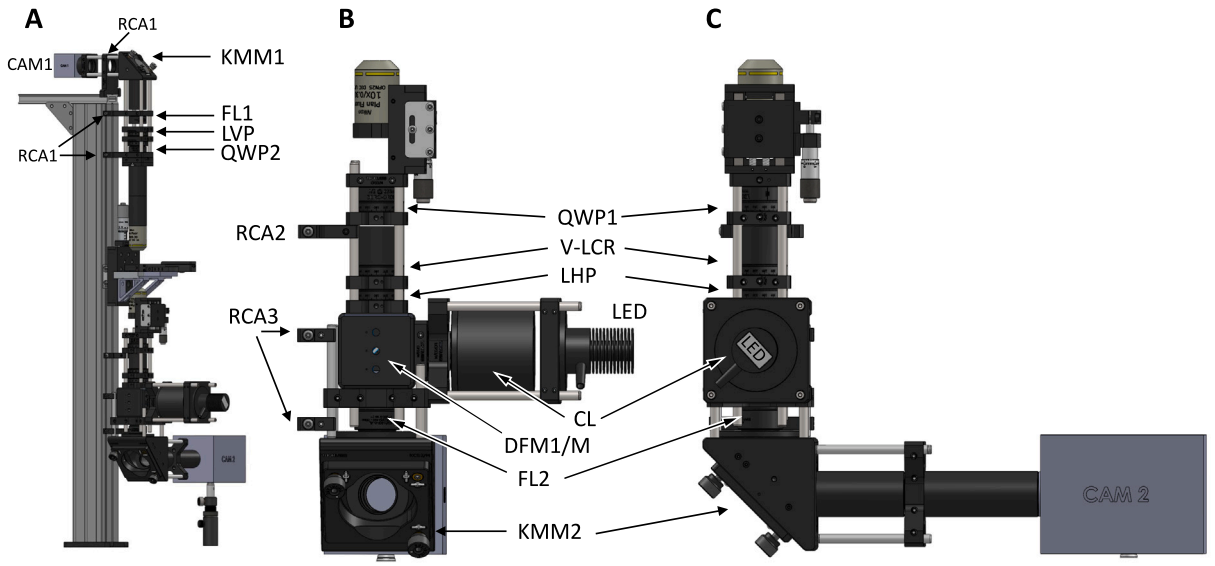

Fig. 2. Optomechanical assembly of the fast adaptive polarimeter. These diagrams have been constructed by combining the CAD files for the different parts, as provided by Thorlabs, and are reproduced here with permission. **A**. Global view of the instrument. Labeled items in the upper module are quarter-wave plate (QWP2), linear vertical polarizer (LVP), field lens (FL1), 90° kinematic mirror mount (KMM1), and camera (CAM1). **B**, **C**. Two magnified orthogonal views of the bottom module. Labeled items are quarter-wave plate (QWP1), variable liquid crystal retarder (V-LCR), linear horizontal polarizer (LHP), LED light source (LED), collimating condenser lens (CL), fluorescence cube assembly (DFM1/M), field lens (FL2), kinematic mirror mount (KMM2), and camera (CAM2). See Movie 1 for a 360 degree rotation of the full assembly.

The total cost of the optomechanical components in the assembly is around 8400€, which is sensibly cheaper than commercial solutions that are slower in response time and do not contemplate the simultaneous fluorescence imaging. Operation of the setup requires the simultaneous use of two grayscale cameras, one scientific-grade, the other fluorescence-grade, that should be added to the other costs, as well as the cost of the LabView license to run the control software. As the image acquisition rate is limited by the performance of the LC retarder, any standard computer hardware that can drive the cameras will be able to operate the instrument. All the mechanical elements of the assembly and most of the optical ones are commercially available from Thorlabs. We have taken advantage of the modular "cage system" to build a stable and modular instrument. A similar construction could be implemented with other modular systems, such as the "cage system" from Edmund Optics or OptoSigma or, for an even lower cost of implementation, using open source hardware platforms such as UC2 [22], among others [23]. Moreover, the modular nature of the instrument allows the two stages, polarimetry and fluorescence, to be built independently, allowing for an easier budget management.

The hardware is computer controlled with custom LabView scripts. For enhanced modularity, we have chosen to use two separate computers, one for the polarimetry, the other one for fluorescence image acquisition. Required synchronization between the two equipments is achieved by means of the DataSocket protocol by National Instruments. This allows to more easily separate the two acquisition modes, and operate them independently. Moreover, users in possession of a high end computer could run the same software within the single equipment, as DataSocket will similarly synchronize the two processes running concurrently in the same system. A schematic of the optical design is shown in Fig. 1. The full optomechanical assembly is shown in Fig. 2. A properly calibrated and aligned instrument, will be of interest in a broad spectrum of fields:

- Liquid crystal researchers will benefit from a realtime assessment of the director field in heterogeneous samples. Simultaneous fluorescence can be employed to map flow patterns, for instance in microfluidic environments.
- The growth of bioorganic crystals can be monitored in real time, assessing the onset of long-range order and incipient crystal orientation. When using confined flow conditions, such as in lab-on-a-chip applications, fluorescent tracers can allow to map the flow surrounding flows.
- Intracellular structures are weakly birefringent, allowing to assess the emergence of long-range order. These observations can be combined with monitoring of standard fluorescent markers.
- Biomimetic active materials prepared with extracts of cytoskeleton proteins have a very low birefringence. The sensitivity of this microscope allows to map the supramolecular ordering without resorting to fluorescent markers, which can be reserved for additional concurrent probes.

3. Design files

3.1. Design files summary

Design filename	File type	Open source license	Location of the file
Adaptive_Polarimeter	LabView (.llb)	CC BY-NC-ND	https://doi.org/10.17605/OSF.IO/BDS26
Fluorescence	LabView (.llb)	CC BY-NC-ND	https://doi.org/10.17605/OSF.IO/BDS26
FullAssemblyCAD	Solidworks	CC BY-NC-ND	https://doi.org/10.17605/OSF.IO/BDS26
Movie1_FullAssembly	Video (.avi)	CC BY-NC-ND	https://doi.org/10.17605/OSF.IO/BDS26
Movie2_Annihilation	Video (.avi)	CC BY-NC-ND	https://doi.org/10.17605/OSF.IO/BDS26
MLC7029_defect annihilation	data (.tif)	CC BY-NC-ND	https://doi.org/10.17605/OSF.IO/BDS26
Movie3_stirring	Video (.avi)	CC BY-NC-ND	https://doi.org/10.17605/OSF.IO/BDS26
5CB under stirring	data (.tif)	CC BY-NC-ND	https://doi.org/10.17605/OSF.IO/BDS26
Movie4_SychAN	Video (.avi)	CC BY-NC-ND	https://doi.org/10.17605/OSF.IO/BDS26
AN_director	data (.tif)	CC BY-NC-ND	https://doi.org/10.17605/OSF.IO/BDS26
Field_Overlay2	ImageJ (.java/.class)	CC BY-NC-ND	https://doi.org/10.17605/OSF.IO/BDS26
Schlieren180	ImageJ LUT (.lut)	CC BY-NC-ND	https://doi.org/10.17605/OSF.IO/BDS26
QTensorFilter	ImageJ (.ijm)	CC BY-NC-ND	https://doi.org/10.17605/OSF.IO/BDS26

- Adaptive_Polarimeter: LabView LLB library (version 2020 or above) with the scripts to control the quantitative polarimetry. The script drives the Thorlabs LCC25 controller (drivers must be installed) and expects a NiDAQX compatible camera. Run the main vi `_Main_Grab.vi`.
- Fluorescence: LabView LLB library (version 2020 or above) with the scripts to control the Fluorescence camera. In this example, it drives the Andor Zyla 4.2MP. Run the main vi `_Main_Grab_Fluo.vi`.
- FullAssemblyCAD: SolidWorks package with the full assembly. Individual components have been downloaded from the Thorlabs website, who owns the copyright of these parts. It is used here with permission.
- Movie1_FullAssembly: Video file rendering in high resolution a 360° rotation of the CAD setup. The video is a uncompressed avi, so it can be opened with any player or with ImageJ. The latter will allow custom zooming.
- Movie2_Annihilation: Video file of the generation and subsequent annihilation of defects in a layer of the liquid crystal MLC7029. Images are cross-polarizer views with an overlay of the orientational field, as measured by our device.
- MLC7029_defect annihilation: Multipage TIFF file corresponding to the previous video. The orientation of the slow axis has been encoded in each pixel as described in the text. To be used with the provided ImageJ tools.
- Movie3_stirring: Video file of a layer of the liquid crystal 5CB under local stirring. Images are cross-polarizer views with an overlay of the orientational field, as measured by our device.
- 5CB under stirring: Multipage TIFF file corresponding to the previous video. The orientation of the slow axis has been encoded in each pixel as described in the text. To be used with the provided ImageJ tools.
- Movie4_SychAN: Video file of a layer of an active liquid crystal made with cytoskeleton proteins, with a very low birefringence. The images in the video correspond to the fluorescence module, and the overlay is the orientation of the slow axis, as captures, simultaneously with our multimodal device.
- AN_director: Multipage TIFF file corresponding to the previous video. The orientation of the slow axis has been encoded in each pixel as described in the text. To be used with the provided ImageJ tools.

- Field_Overlay2: Java plugin for ImageJ/FIJI. It should be copied into the plugins folder (or in a subfolder) and compiled with Plugins/Compile and Run. If your installation is not able to compile plugins, then we provide, in the repository, the two .class files that the compilation generates, `Field_Overlay2.class` and `Field_Overlay2\$CustomCanvas.class`.
- Schlieren180: Grayscale lookup table where the graylevel of each index corresponds to the scaled transmission intensity between crossed polarizers. This LUT is to be loaded into FIJI to visualize the orientation-encoded slow axis images in simulated crossed polarizer view.
- QTensorFilter: FIJI macro used to remove high frequency spatial noise from the orientation-encoded slow axis images obtained from measurements with the adaptive polarimeter. Spatial filters cannot be directly applied on orientation maps because of discontinuities. This macro obtains the tensorial order parameter for each pixels, applies a spatial filter, and recovers the smoothened orientation field.

4. Bill of materials

We include below a complete bill of materials with the optomechanical and optical components required to build the complete setup. The materials are grouped by category. This list includes two standard-quality cameras for polarimetry and fluorescence imaging. Please, refer to the CAD assembly files for details of the assembly and to plan modifications of this proposed setup. Prices are up to date in July 2023.

Designator	Component	Num	Unit cost Euros	Total cost Euros	Source of materials	Material type
Rail	66 mm Construction Rail, L = 750 mm	1	107.42	107.42	Thorlabs XT66-750	Optomech.
Platform	66 mm Double dovetail rail, L = 500 mm	1	47.65	47.65	Thorlabs XT66DP-500	Optomech.
Mounting plate	Vertical Mounting Plate for 66 mm Optical Rail	1	37.59	37.59	Thorlabs XT66P1	Optomech.
Clamp	Right angle clamp for 66 mm rails	2	52,40	104.79	Thorlabs XT66RA1	Optomech
Rail-to-cage plate 30 mm	SM1-Threaded 30 mm Cage Plate for 66 mm Rails	3	49,43	148,29	Thorlabs RCA1	Optomech.
Rail-to-cage bracket 30 mm	Mounting bracket to couple 30 cage to 66 mm rail	1	51.90	51.90	Thorlabs RCA2	Optomech.
Rail-to-cage bracket 60 mm	Mounting bracket to couple 60 cage to 66 mm rail	2	51,90	103.80	Thorlabs RCA3	Optomech.
Plate adapter	Adapter to couple 30 mm and 60 mm cage assemblies	3	41.29	123.86	Thorlabs LCP33	Optomech.
Cage plate	SM1-Threaded 30 mm Cage Plate, 0.35" Thick	4	17.36	69.43	Thorlabs CP33/M	Optomech.
Rods 6"	6 mm S. Steel rods for cage assemblies, 6" long	16	8.51	136.08	Thorlabs ER6	Optomech.
Rods 4"	6 mm S. Steel rods for cage assemblies, 4" long	2	6.97	13.94	Thorlabs ER4	Optomech.
Rods 3"	6 mm S. Steel rods for cage assemblies, 3" long	16	6.16	98.62	Thorlabs ER3	Optomech.
Rods 1"	6 mm S. Steel rods for cage assemblies, 1" long	8	4.72	37.74	Thorlabs ER1	Optomech.

Designator	Component	Num	Unit cost Euros	Total cost Euros	Source of materials	Material type
1" Lens tube	SM1 lens tube, 1" long	1	14.01	14.01	Thorlabs SM1L10	Optomech.
1" Lens tube	SM1 lens tube, 2.5" long	1	21.59	21.59	Thorlabs SM1S25	Optomech.
1" Spacer	SM1 lens tube spacer, 1" long, external threads	1	13.03	13.03	Thorlabs SM1S10	Optomech.
1" Tube coupler	SM1 tube coupler, external thread	1	19.56	19.56	Thorlabs SM1T3	Optomech.
2" Tube coupler	SM2 Coupler, External threads	1	36.79	36.79	Thorlabs SM2T2	
2" Lens tube	SM2 lens tube, 1.5" long	1	30.35	30.35	Thorlabs SM2L15	Optomech.
2" Lens tube	SM1 lens tube, 2" long	2	16.22	32.45	Thorlabs SM1L20	Optomech.
Adapter tube	Adapter with External SM2 Threads and Internal SM1 Threads	2	25.94	51.88	Thorlabs SM2A6	Optomech.
Adapter tube	Adapter with External SM1 Threads and Internal SM2 Threads	2	25.31	50.62	Thorlabs SM1A2	Optomech.
C-mount	Adapter External C-Mount Threads and Internal SM1 Threads	2	19.05	38.10	Thorlabs SM1A9	Optomech.
1" Mirror mount	Elliptical mirror Kinematic Mount	1	198.59	198.59	Thorlabs KCB1E/M	Optomech.
2" Mirror mount	Right-angle kinematic mirror mount for 60 mm cage system, with Tapped Cage Rod Holes	1	170.22	170.22	Thorlabs KCB2/M	Optomech.
Rotating mount	30mm Cage Rotation Mount for Ø1" Optics, SM1 Threaded	5	85.49	427.45	Thorlabs CRM1T/M	Optomech.
Focus stage	Travel Manual Translation Stage for 30 mm Cage Systems	1	452.05	452.05	Thorlabs CT1	Optomech.
Fluorescence block	Detachable fluorescence cube for 30 mm cage system	1	377.79	377.79	Thorlabs DFM1/M	Optomech.
XY stage	XY translation stage and sample holder	1	358.07	358.07	Thorlabs XYF1/M	Optomech.
Post holder	Translating 12,7 mm post holder	1	62.46	62.46	Thorlabs PH3T/M	Optomech.
Post	12,7 mm post, 75 mm.	1	5.60	5.60	Thorlabs TR75/M	Optomech.

Designator	Component	Num	Unit cost Euros	Total cost Euros	Source of materials	Material type
Field lens	Achromatic Doublet (f = 200 mm, 1" diameter) with SM1-Threaded Mount	2	103.75	207.50	Thorlabs AC254-200-A-ML	Optics
Condenser	2" Aspheric condenser	1	44.73	44.73	Thorlabs ACL50832U	Optics
Elliptical mirror, 1"	Broadband Dielectric Elliptical Mirror	1	116.20	116.20	Thorlabs BBE1-E02	Optics
Mirror, 2"	Broadband Dielectric Mirror (2" diameter)	1	149.40	149.40	Thorlabs BB2-E02	Optics
Quarter-wave plate	Polymer Zero-Order Quarter-Wave Plate (670 nm, 1" diameter)	2	286.89	573.78	Thorlabs WPQ10E-670	Optics
Polarizer	Linear polarizer (1" diameter)	2	96.34	192.68	Thorlabs LPVISE100-A	Optics
Fluorescence filter set	Cy5 Fluorescence filter set	1	770.00	770.00	Edmund Optics 67-010	Optics
LC retarder	Compensated Half-Wave LC Retarder	1	794.00	794.00	Thorlabs LCC1411-A	Optics
LC controller	Liquid crystal compensator controller	1	1375.19	1375.19	Thorlabs LCC25	Electronics
LED	660 nm LED module with SM1 thread	1	228.67	228.67	Thorlabs M660L4	Optics
LED driver	T-Cube LED Driver	1	316.53	316.53	Thorlabs LEDD1B	Electronics
Objective	Nikon CFI 60 10x objective, 7 mm WD	2	190.96	190.96	Local supplier	Optics
Camera	Camera Blackfly GigE Teledyne	1	1000	1000	Local supplier, BFLY-PGE-50S5M-C	Electronics
Camera	Fluorescence camera Andor Zyla 4.2MP	1	12000	12000	Local Supplier	Electronics

5. Build instructions

Optomechanical assembly

Fine adjustment of the optical devices

In order to achieve the desired precision when obtaining the local order of a birefringent sample with the instrument described here, it is imperative to precisely calibrate the orientations of all the optical elements, especially when imaging low-birefringent samples. This is better performed prior to assembling the instrument. Notice that the manufacturer specifies the fast axis of polarizing or birefringent optical elements, but precision is often not enough. For example, we have found discrepancies of up to 20° in some of our purchased compensators.

To determine optical fast axes, we use a custom made optical setup (see Fig. 3) that includes a monochromatic red laser light source (Monocrom, M-Series VIS 6335 laser diode and PSLDM5-PWR-M power supply), a polarizing beam-splitting prism (Thorlabs, PBS253) and a light power meter (Thorlabs, PM100USB with an S120VC sensor) controlled with the Optical Power Meter Utility from Thorlabs. The prism separates the p- and s-polarized waves by transmitting the former and reflecting the latter at 90°. The

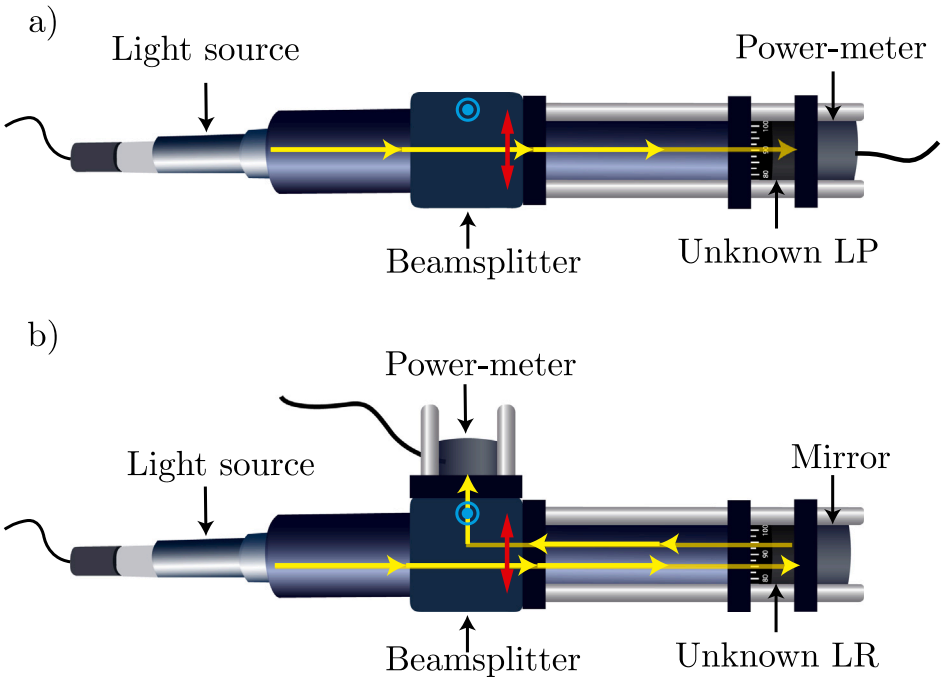

Fig. 3. Calibration of the optical devices. Sketches that represent the setup used to determine the polarization direction of a linear polarizer (LP) (a) and the fast axis of a linear retarder (LR) (b). Red (p-polarization) and blue (s-polarization) arrows indicate light polarization. The yellow arrow represents the light path. (For interpretation of the references to color in this figure legend, the reader is referred to the web version of this article.)

laser source is rotated to maximize transmittance through the prism (p-polarization). The devices are assembled using Thorlabs cage optomechanical hardware, as illustrated in Fig. 3. Optical elements to be calibrated are already mounted in a Thorlabs CRM1T rotating mount, that will be directly assembled in the polarimeter after this adjustment. Notice that we have two alternative configurations, depending on whether we want to adjust a LP or a QWP. For the latter, a first surface mirror (Thorlabs ME1-G01) is also required. Below, we explain the details of each assembly and calibration.

Linear polarizers. The polarization axis of a linear polarizer is readily obtained by placing it after the polarizing beam-splitter and before the power-meter and by seeking the orientation of minimum transmission, i.e., the orientation with the lowest light intensity reaching the detector (see 3.a). For better precision, we measure the transmittance 20 degrees below and above this estimated orientation and fit the data to improve the determination of the optimal angle. At this disposition, the linear polarizer is at 90° from the beam-splitter's incidence plane. See Appendix for detailed Muller calculus.

Linear retarders (QWP and LCR). We calibrate all the quarter wave plates using the setup illustrated in Fig. 3.b. With this assembly, the p-polarized light exiting the prism crosses the retarder, collides with the mirror, travels back though the retarder, and reaches the prism again. In this configuration, the detector is placed to measure the s-polarized light, reflected by the prism. One can demonstrate that, in this configuration, the intensity reaching the detector is $I(\theta) \propto (1 - \cos 4\theta)$, where θ is the orientation of the fast axis of the quarter wave plate. See Appendix for detailed Muller calculus.

By taking as a reference the fast axis direction provided by the manufacturer, we rotate the wave plate to obtain a maximum ($\theta = 45°$) or a minimum ($\theta = 0$) intensity at the detector, depending on the optical element. As we do to align the linear polarizers, here we measure intensities for a range of angle above and below the estimated optimal value, and fit the data to optimize the alignment. Notice that, for the LCR, we must keep a suitable voltage for its retardance to be one quarter of the laser wavelength.

Backbone assembly.

The 66 mm dovetail rail column is first secured on an optical table. Then, the different cage coupling elements (RCA1, RCA2, and RCA3) are secured as shown in Fig. 2. Cage rods will be placed together with the different optical elements.

Assembly of the fluorescence module.

A 60 mm cage plate is placed between the two RCA2 couplers, and the three elements are secured in position. The cage cube that will hold the CY5 filter set inside (DFM1/M) is then secured on top of the 60 mm cage plate. Notice that the emission filter from the filter set will also serve to condition the light that will travel through the polarimetry elements. The birefringent components are designed for a wavelength of 635 nm, which is compatible with the transmission band of our filter set (604–644 nm). It is crucial that the fluorescence cube is placed before any polarization element, as light might be slightly unpolarized by the dichroic mirror. The LED light source is then assembled on the right port of the cube. The LED output is nearly collimated using a 50 mm glass aspheric lens. Final adjustment of the LED-collimator distance will be later performed to optimize the illumination homogeneity of the field of view. A field lens and a mirror (on a kinematic mount) is finally assembled on the bottom port of the fluorescence cube,

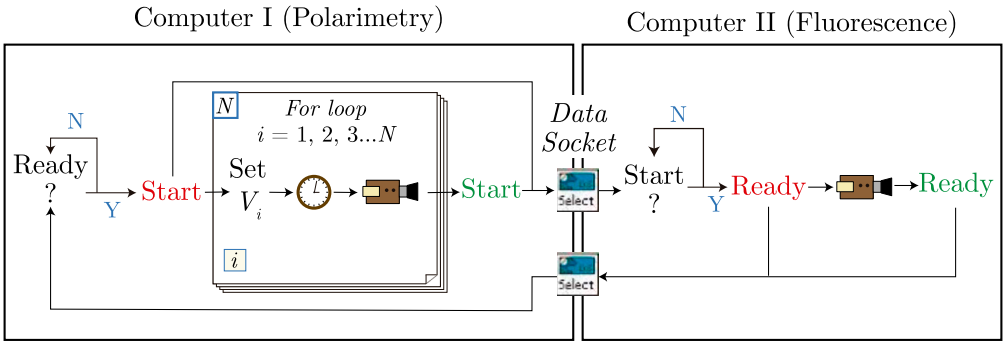

Fig. 4. Flow diagram for the cameras synchronization protocol.

with a camera secured with the sensor at approximately 200 mm from the field lens. The camera should have a suitable support to ensure that no stress is exerted on the optical assembly.

Assembly of the polarimetry module.

Once the fast axes of the optical devices are known (see above), the setup is assembled in steps (see Fig. 1). To optimize the alignment and check for small errors, we mount the instrument device by device, starting with the two crossed polarizes one at 0° and the other at 90° and checking that the light intensity reaching CAM1 is minimal at such disposition. Then, we incorporate the variable LCR to the setup with an orientation of 45° from the polarizers. With this configuration, the intensity must be maximal. Next, we assemble the QWP at 0°, ensuring that the intensity is minimal in this case. We finally add the last QWP at 45° right before the LVP. In this disposition, the intensity arriving at the detector must be maximal.

Device and software setup

Device setup.

The user should ensure that both cameras are on and are correctly detected by LabView (this can be checked within the NI-MAX utility or using any sample VI provide by the camera manufacturer). Similarly, the drivers for the variable LCR controller should be properly installed and tested, following the manufacturer instructions.

Software setup.

The synchronization of both computers and, in turn, of both cameras and the variable LCR is attained with the DataSocket protocol within LabVIEW, which enables the interchange of data, in our case two boolean variables (true/false variables, `Start` and `Ready`) between the two computers. When the user starts the measurement process, both boolean variables are set to true, *Computer I* sends the `Start` (true) variable to *Computer II*, and *Computer II* sends `Ready` (true) to *Computer I*, and the measurement process begins. *Computer I*, once it reads a true value of `Ready`, sets `Start` to false and enters the For loop. For each For cycle, a different voltage is applied to the variable LCR, then the system waits for at least 120 ms (the optimal settling time for the variable LCR, see below) and acquires an image. Once the system exits the For loop, it sets the `Start` boolean to true, which is read by *Computer II*, which has been awaiting until it receives a true value of the `Ready` variable, changes the `Ready` variable to false, acquires a fluorescence image, and changes `Ready` back to true. In this way, `Ready` and `Start` are continuously exchanged between both computers and control the acquisition time. This process is depicted in Fig. 4 and is repeated until the user stops the acquisition. Note that this synchronization procedure can also be performed using only one computer. In this case, we used two separate computers to prevent performance limitations.

To ensure optimal synchronization between both image acquisition processes, we also store the acquisition time of each frame for both imaging techniques and then compare both times. Fluorescence/polarimetry frames with a time offset between polarimetry/fluorescence frames surpassing a threshold (which will depend on the dynamic behavior of the system under observation) are discarded.

Calibration and testing

Spatial alignment of the polarimetry and fluorescence modules.

Spatial registry between the two microscope modules is also crucial. To determine the lateral offsets between the fluorescence and polarimetry images, we use a microscope stage calibration slide. By imaging the ruler simultaneously with both imaging techniques and measuring the position of several points in the ruler relative to each field of view, we can finally obtain the spatial offsets, which will be taken into account into any further simultaneous analysis of the two type of images.

Final adjustment of the combined optical elements.

After the assembly of the instrument, we fine tune and correct the presence of small misalignments between the optical devices. For the sake of simplicity, we ignore errors coming from the orientation of the two LP and from the retardance of the compensators, which are usually fairly well characterized. Thus, to assess the misalignments, we measure the light intensity when the retardance of the variable LCR is set at 0, $\pi/2$, π, and $3\pi/2$ without a sample. Afterwards, we extract the deviations from the theoretical orientations

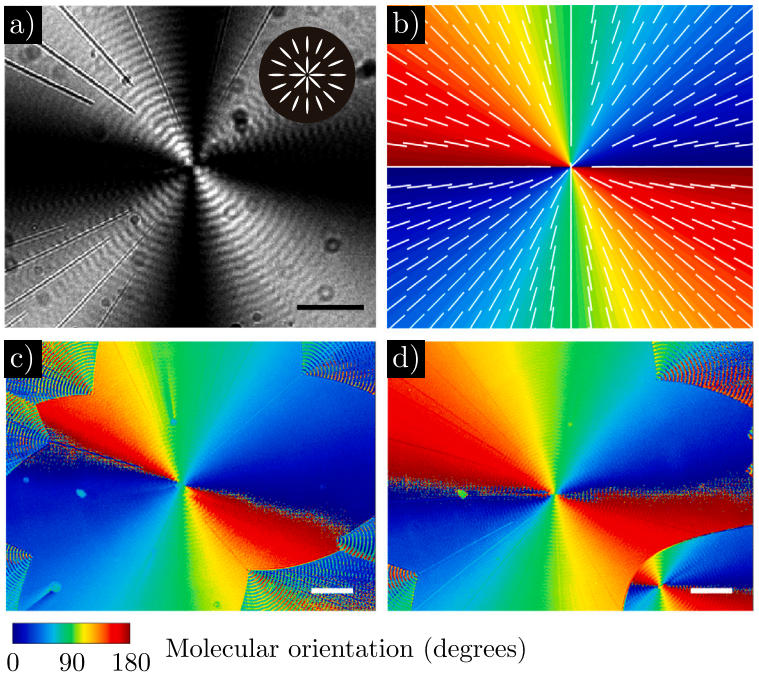

Fig. 5. Measurements of D-mannitol spherulites. (a) The alignment of mannitol molecules forms spherulites, which appear as a Maltese cross under an optical microscope with crossed polarizers. The top inset represents the local alignment of a spherulite. The scale bar is 100 μm. (b) Theoretical colormap indicating the orientation of an ideal spherulite. (c),(d) Colormaps representing the measured orientation of a spherulite using a LCR-based polarimeter with (c) and without (d) alignment errors between the optical elements.

of the variable LCR (δ_0) and the first and second QWP (δ_1 and δ_2, respectively) with the following relations (see Appendix for detailed Mueller calculus):

$$\delta_2 = \frac{1}{2}\frac{I(\pi/2) - I(3\pi/2)}{I(\pi/2) + I(3\pi/2)}, \tag{1}$$

$$(\delta_1 - \delta_0) = \frac{1}{2}\frac{I(0) - I(\pi)}{I(0) + I(\pi)} \tag{2}$$

The two deviations δ_0 and δ_1 cannot be isolated from each other. As a consequence, we must correct them by trial and error.

To ascertain the correct assembly of the instrument, we measure the local fast axes of a thin polycrystalline sample of twisted D-mannitol lamellae displaying birefringent spherulites. Samples containing these structures are very convenient for calibrating birefringence imaging techniques because the molecules are organized in a radial pattern, displaying a Maltese cross under a microscope (see Fig. 5.a). A detailed explanation of how to prepare samples with this spherulitic material can be found in [24]. An ideal spherulite features local orientations as the ones shown in Fig. 5.b. However, if the optical elements in the birefringent imaging technique are not accurately aligned, the measured fast axes diverge from this ideal disposition, and, therefore, a more accurate correction of the offsets is required (see Fig. 5c,d).

Liquid Crystal Retarder performance.

The bottleneck in the temporal performance of the instrument is the settling time of the LCR (τ_{LCR}) upon changing its applied voltage. Values quoted by the manufacturer are typically underestimated, and must be calibrated for better performance. During operation of the microscope, if the LCR voltage is changed before the device has properly stabilized at the previous voltage value, significant errors in the fast axis determination are obtained. We obtain a first estimation of τ_{LCR} by observing the settling in the grayscale intensity when captured by the polarimeter when the voltage of the LCR is changed, in the absence of any sample (Fig. 6.a).

To estimate the optimal value for τ_{LCR}, we use a custom-made liquid crystal cell with planar alignment along a precisely-known direction. Alternative birefringence sample could be employed, but their fast axis should be known with great precision.

We proceed to repeatedly measure the orientation of the LC cell fast axis using images captured at three different configurations of the LCR, which we choose to be $\psi_A = 0$, $\psi_B = \pi/2$, and $\psi_C = \pi$ to simplify the analysis (see Section 7), but testing different waiting times between voltage changes and image acquisition for each measurement. As shown in 6.b, measurements with a waiting time < 120 ms yield an erroneous orientation with considerable uncertainty. We, therefore, establish 120 ms as the optimal settling time between subsequent voltages.

Finally, in order to further optimize the acquisition rate of the microscope, we will employ a triangular sequence of voltages instead of a sawtooth sequence. Indeed, the sequence ABCABCABC... is less effective than ABCBABCBAB... Since the acquisition order of the three LCR configurations required for quantitative polarimetry is not relevant, the third measurement from a given frame is employed by the control software as the first measurement from the next.

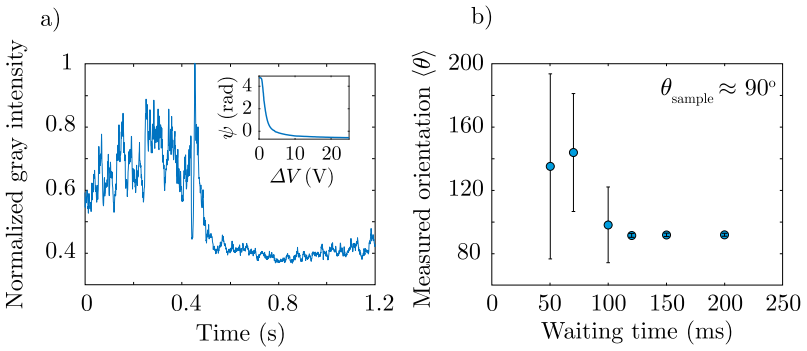

Fig. 6. Optimal settling time. (a) Normalized gray intensity of micrographs acquired with the polarimeter without a sample while changing the applied voltage to the LCR. In the beginning, $\Delta V = 0$. Then, around ~ 0.45 s, we apply a voltage $\Delta V = 4.4$ V. The LCR requires around $\sim$ 100–200 ms to stabilize its retardance. The inset displays the dependence of the variable LCR's retardance ψ with the applied voltage ΔV. At $\Delta V = 0$, the gray intensity fluctuates more than at $\Delta V = 4.4$ V because the LCR retardance is more sensitive to voltage fluctuations at small voltages than at large voltages. (b) Measurements of a planar LC cell using different waiting times (time between the voltage application and the image acquisition). All the measurements are performed using the optimal three different configurations of the variable LCR ($\psi_A = 0$, $\psi_B = \pi/2$, $\psi_C = \pi$). The LC cell is oriented with its fast axis lying at 90°. The plotted data are the average of 10 different measurements. Error bars indicate standard deviations.

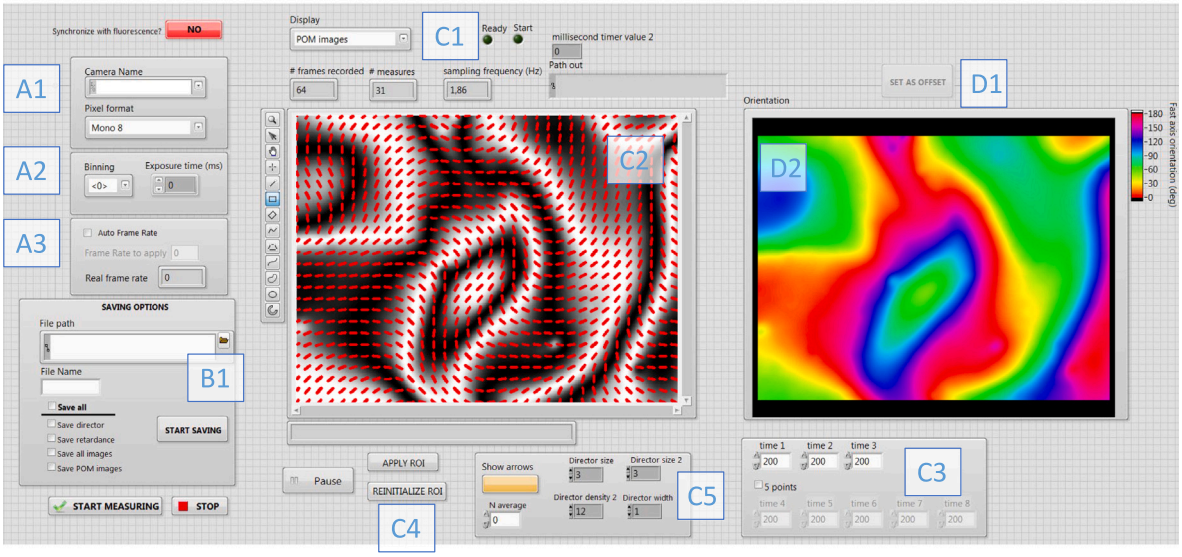

Fig. 7. User front end of the LabView program used to drive the polarimetry module. Block A sets up the basic parameters of the used camera. Block B determines the location and the information saved for further processing. Block C controls the polarimetry measurements, such as the region of interest and the time intervals between successive configurations of the LCR. Block D allows to display, in real time, the processed polarimetry data.

6. Operation instructions

6.1. Image acquisition and in-situ, real-time processing

Polarimetry

The polarimetry module is driven by a custom LabView script, whose Front Panel is shown in Fig. 7. Prior to starting the program, the user must specify the basic features of CAM1 (Fig. 2), such as the device name and pixel depth (A1), binning and exposure time (A2) or automatic frame rate can be selected (A3). The user must also specify type and location of data to store in the disk and a base file name for the experiment(B1). Data saving can be started at any time once the experiment is running, allowing for proper image adjustment. The user must also specify whether the measurement will involve three points (default) or five points for polarimetry measurements (see Section 7). Only the former allows the maximum rate of 2.5 frames per second. The user must also specify the time (in ms) between adjustments of the LCR (C3), with 120 ms being the minimum time to ensure correct polarimetry measurements (see above). Finally, the user must also specify whether polarimetry and fluorescence microscopy will be performed simultaneously, in which case the two measurements must be synchronized, as described in the text (selector at the top left of the Front Panel).

Once the program is running, panel C2 displays the data selected in control C1, such as the raw, unprocessed polarimetry data, or the processed data reconstructing the image between crossed polarizers (as shown in Fig. 7). This allows to correctly adjust image focus and placement and to specify the region of interest. Optionally, the computed orientational field (slow axis orientation) can be overlaid on the image in panel C2, with a segment size and density that is user-selectable (C5). The user can draw a ROI directly in the image panel (C2), choose this ROI for image acquisition, or reset it to full screen (C4). Data is processed in real time to display the slow optical axis of the birefringent sample in panel D2 as a color map. The signal-to-noise ratio can be improved by subtracting a background image captured using button D1. Usually, this image is selected by placing an empty cell similar to the one that will contain the sample in the sample holder, and compensates for small residual birefringence or misalignment of the optical components.

Fluorescence

The fluorescence camera CAM2 is operated by an independent LabView program that we run on a separate computer. The sample program provided here performs acquisition using an Andor Zyla 4.2MP camera, which uses a proprietary implementation of the camera controls. The reader will have adapt that program to the fluorescence-grade camera of their choice. Simultaneous acquisition of polarimetry and fluorescence is achieved using the DataSocket communication protocol. Alternatively, the two acquisition threads could be run on a single performing computer with no changes in the control programs. The user should refer to NI DataSocket manuals and tutorials for the correct setup of the communications.

6.2. Ex-situ data analysis and visualization

Output data format

Polarimetry data are output as two sets of unsigned 16-bit image sequences. In the orientation field, each pixel contains the local orientation of the slow axis (in the range 0 .. 180 degrees) multiplied by 256, for enhanced numerical resolution. In the retardance field, each pixel contains the local retardance (in the range 0 .. 160 nm) multiplied by 256, also for enhanced numerical resolution. In the case of fluorescence microscopy, output 16-bit images contain the fluorescence intensity, in arbitrary units.

ImageJ tools for visualization and processing

Image sequences can be directly imported into FIJI for further processing and visualization. It is often convenient to filter the high frequency noise that results from fast image acquisition. While common filtering strategies can be employed for the retardance maps, one has to be more careful when applying a spatial filter to the orientation map, $\theta(x, y)$, as the prescription that angles be given in a 180 degree range results in discontinuity lines when the orientation suddenly changes from 0 to 180 degrees or viceversa. A spatial filter would erroneously smooth those discontinuity lines. Instead, we propose a filter based on the tensorial order parameter, whose components are a function of the trigonometric functions of 2θ. To use this tool, import the orientation data as an image stack in FIJI and open the macro file QTensorFilter.ijm (available in the repository). You can specify the width of the Gaussian Blur (parameter FilterSigma, which is set at 4 pixels by default) and then run the macro. It will create a new 16-bit stack with the high frequency noise removed and the angular value in the same format as the original data. Notice that this filter uses some scripting tools that may not be directly available in all ImageJ installations, but that is available in an up-to-date FIJI implementation.

Inside FIJI, angular data can be better visualized by choosing a suitable LUT (Lookup table) to convert pixel values into grayscale. The default linear gray scale LUT can be replaced by the Spectrum LUT by selecting `Image > Lookup Tables > Spectrum`. This LUT has been used in some displayed images in Section 8, and has the advantage of having the same color scheme for the lowest and for the highest value, those removing the jump discontinuity in the angular data. It is also practical to simulate the sample visualization between crossed polarizers. For this purpose, you can use the LUT Schileren180.lut (available in the repository). To apply this LUT, select `Color > Edit LUT > Open ''Schlieren180.lut'' > OK`.

Additionally, we provide a FIJI/ImageJ plugin that allows to visualize the orientational field as a vector overlaid on top of the image data. The plugin is called `Field_Overlay2`. The corresponding Java file should be copied into the plugins folder and compiled or, alternatively, the two .class files provided in the repository should be copied into the plugins folder. This plugin should be used once the stack with slow axis orientations is opened and visualized with the suitable LUT. The stack will overlay a field of red arrows corresponding to the local underlying orientation. A brief menu prints in the Results windows with basic instructions with key combinations to change the size, density, and arrow type of the field. Notice that you can zoom the images (using FIJI/ImageJ zoom tool) for better visualization of the orientational field. Finally, the stack can be rendered as an RGB stack with the red arrows irreversibly drawn on the image. We have used this tool to generate the orientational fields in Section 8.

7. Optical principles and analysis of the polarimetry data

Light polarization can be modified with optical devices, such as linear polarizers and retarders (or compensators). The effect of a series of stacked devices can be computed using the Mueller calculus formalism (Fig. 8). Each device is characterized by a real 4×4 matrix that operates on the 4-component Stokes vector of light, where

$$S_0 = E_x^2 + E_y^2 \tag{3}$$

$$S_1 = E_x^2 - E_y^2 \tag{4}$$

$$S_2 = 2E_x E_y \cos\delta \tag{5}$$

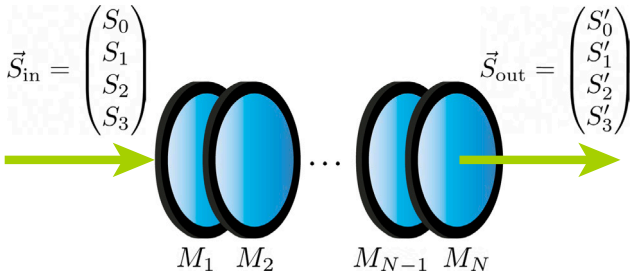

Fig. 8. Light polarization with optical devices — Diagram showing a beam with a Stokes vector $\vec{S}_{\text{in}}$ crossing different optical elements with Mueller matrices M_1, M_2, …, M_{N-1}, M_N. The emergent beam comes out with a different polarization characterized by a stokes vector $\vec{S}_{\text{out}}$.

Table 1
Sequence of Mueller matrices modeling the sequence of optical elements in the quantitative polarimetry microscope.

Emergent light

$$\vec{S}_{\text{out}} = \begin{pmatrix} S'_0 \\ S'_1 \\ S'_2 \\ S'_3 \end{pmatrix} = \text{Linear vertical polarizer} \cdot \text{QWP fast axis at } 45° \cdot \text{Sample} \cdot \text{QWP fast axis at } 0° \cdot \text{LCR fast axis at } 45° \text{ with retardance } \psi \cdot \text{Linear horizontal polarizer} \cdot \text{Incident light}$$

Linear vertical polarizer

$$\frac{1}{2}\begin{pmatrix} 1 & -1 & 0 & 0 \\ -1 & 1 & 0 & 0 \\ 0 & 0 & 0 & 0 \\ 0 & 0 & 0 & 0 \end{pmatrix}$$

QWP fast axis at 45°

$$\begin{pmatrix} 1 & 0 & 0 & 0 \\ 0 & 0 & 0 & -1 \\ 0 & 0 & 1 & 0 \\ 0 & 1 & 0 & 0 \end{pmatrix}$$

Sample

$$\begin{pmatrix} 1 & 0 & 0 & 0 \\ 0 & \cos^2 2\theta + \sin^2 2\theta \cos\delta & (1-\cos\delta)\cos 2\theta \sin 2\theta & -\sin 2\theta \sin\delta \\ 0 & (1-\cos\delta)\cos 2\theta \sin 2\theta & \sin^2 2\theta + \cos^2 2\theta \cos\delta & \cos 2\theta \sin\delta \\ 0 & \sin 2\theta \sin\delta & -\cos 2\theta \sin\delta & \cos\delta \end{pmatrix}$$

QWP fast axis at 0°

$$\begin{pmatrix} 1 & 0 & 0 & 0 \\ 0 & 1 & 0 & 0 \\ 0 & 0 & 0 & 1 \\ 0 & 0 & -1 & 0 \end{pmatrix}$$

LCR fast axis at 45° with retardance ψ

$$\begin{pmatrix} 1 & 0 & 0 & 0 \\ 0 & \cos\psi & 0 & -\sin\psi \\ 0 & 0 & 1 & 0 \\ 0 & \sin\psi & 0 & \cos\psi \end{pmatrix}$$

Linear horizontal polarizer

$$\frac{1}{2}\begin{pmatrix} 1 & 1 & 0 & 0 \\ 1 & 1 & 0 & 0 \\ 0 & 0 & 0 & 0 \\ 0 & 0 & 0 & 0 \end{pmatrix}$$

Incident light

$$\begin{pmatrix} S_0 \\ 0 \\ 0 \\ 0 \end{pmatrix}$$

$$S_3 = 2E_x E_y \sin\delta. \tag{6}$$

Here, E_x and E_y are the amplitude of the components of the electric field of polarized light that travels along the z-axis, and δ is the phase shift, or retardance, between both components.

In the quantitative polarimetry microscope, light from the LED source travels through the sequence of devices (Fig. 1): Linear Horizontal Polarizer (LHP) → Liquid Crystal Retarder (with variable retardance ψ and fast axis at 45° from LHP) → Quarter Wave Plate (QWP, fast axis parallel to LHP) → Sample → QWP (with fast axis at 45° from LHP) → Linear Vertical Polarizer (LVP) → Detector (camera).

In order to predict light modulation with this set up we performed the appropriate Mueller calculus. We consider that the optical properties of the birefringent transparent materials we will study can be simulated by a linear retarder whose fast axis is rotated at an angle θ with respect to the LHP:

$$M_{\text{sample}} = R(-\theta) M_{\text{LR}} R(\theta) \tag{7}$$

The Mueller calculus for the set up is shown in Table 1 For the sake of clarity, the name of each element is written above the appropriate matrix.

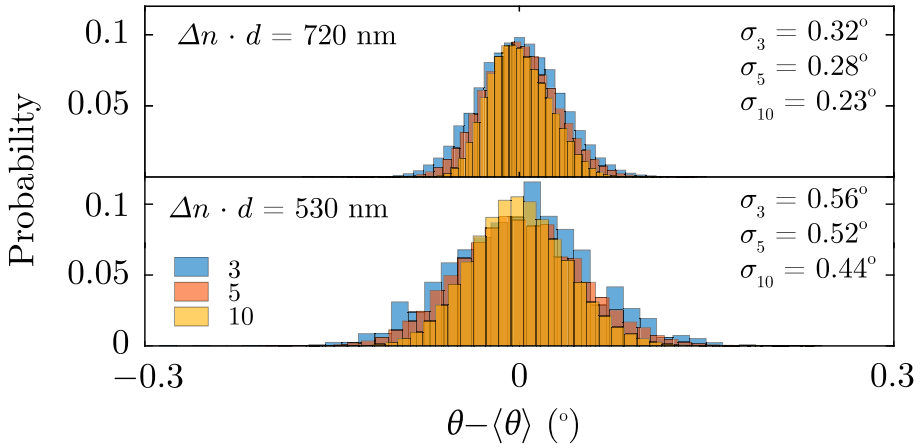

Fig. 9. Measurements using different number of fitting points. Histograms showing the probability to measure a fast axis orientation θ using homogeneous samples with $\Delta n \cdot d = 720$ nm (top) and 530 nm (bottom). We measure the fast axis using either 3, 5, or 10 images acquired at different configurations of the variable LCR (different ψ values). The standard deviations of each histogram are indicated as insets in both panels. The test samples are quarter wave plates from a Nikon 50i Pol microscope.

The detector (camera CAM2) is only sensitive to light intensity (I), which corresponds to the Stokes parameter S_0'. For this system, the intensity measured at each picture element is:

$$I = \begin{pmatrix}1 & 0 & 0 & 0\end{pmatrix} \cdot \vec{S}_{\text{out}} = \frac{1}{4} S_0 (1 + \sin 2\theta \sin\delta \cos\psi - \cos 2\theta \sin\delta \sin\psi) \tag{9}$$

By acquiring images at different values of ψ (retardance of the LCR) and using the equation

$$I = a + b\cos\psi + c\sin\psi, \tag{10}$$

where

$$a = I_0, \qquad b = I_0 \sin 2\theta \sin\delta, \qquad c = -I_0 \cos 2\theta \sin\delta, \tag{11}$$

one obtains the local fast axis orientation (θ) and the local retardance (δ) as

$$\theta = \frac{1}{2}\text{atan2}\left(\frac{b}{-c}\right), \qquad \delta = \arcsin\left(\frac{\sqrt{b^2 + c^2}}{a}\right). \tag{12}$$

Here, atan2 is the four-quadrant inverse tangent. Since δ is obtained from the inverse sine function, the maximum retardance for unambiguous measurement is $\delta = \pi/2$, which corresponds to $\Delta nd = \lambda/4$, where $\Delta n = n_e - n_o$ is the birefringence, with n_e and n_o the refractive indexes of the extraordinary and ordinary ray, respectively, d is the thickness of the anisotropic specimen and λ stands for the wavelength of the propagating length. Moreover, in the usual case where $\Delta n > 0$, the optic axis will be oriented at $\theta + \pi/2$. These results are valid for a transparent sample, with a Mueller matrix given by Eq. 1. For an absorbing sample having also linear dichroism, the detected intensity would take a more complicated form and the birefringence could not be obtained from the equations above. In such a case, other quantitative microscopy implementations, measuring the complete Mueller matrix [1,3] would be more suitable.

Note that, with the above analysis, three measurements at three different values of ψ will be the minimum required to measure θ and δ. The optimum values of ψ when performing a measurement based on three intensity acquisitions are 0°, 90°, and 180°. For systems that are static or have a slow enough dynamics, additional measurements can be obtained, which will increase the signal-to-noise ratio by fitting the parameters a, b, and c above, although the improvement is marginal (Fig. 9).

Background correction

In practice, there is always background noise due to thermal fluctuations, small misalignments of the optical elements, spatial variations in the retardance of waveplates, etc. To maximize the performance and measure materials with very small birefringences, we always capture a blank prior to initiating each sample birefringence imaging. To do so, we remove or replace the sample with a transparent isotropic thin material, such as a clean glass slide, similar to the ones used for the real sample, and retrieve the a_{blank}, b_{blank}, and c_{blank} (note that, in an optically ideal system, b_{blank}, and c_{blank} should be zero). These parameters are later subtracted from the sample's b, and c parameters pixel by pixel as:

$$b' = \frac{b}{a} - \frac{b_{\text{blank}}}{a_{\text{blank}}} \quad , \qquad c' = \frac{c}{a} - \frac{c_{\text{blank}}}{a_{\text{blank}}}. \tag{13}$$

With this, Eq. (12) becomes

$$\theta = \frac{1}{2}\text{atan2}\left(\frac{b'}{-c'}\right), \qquad \delta = \text{asin}\left(\sqrt{b'^2 + c'^2}\right). \tag{14}$$

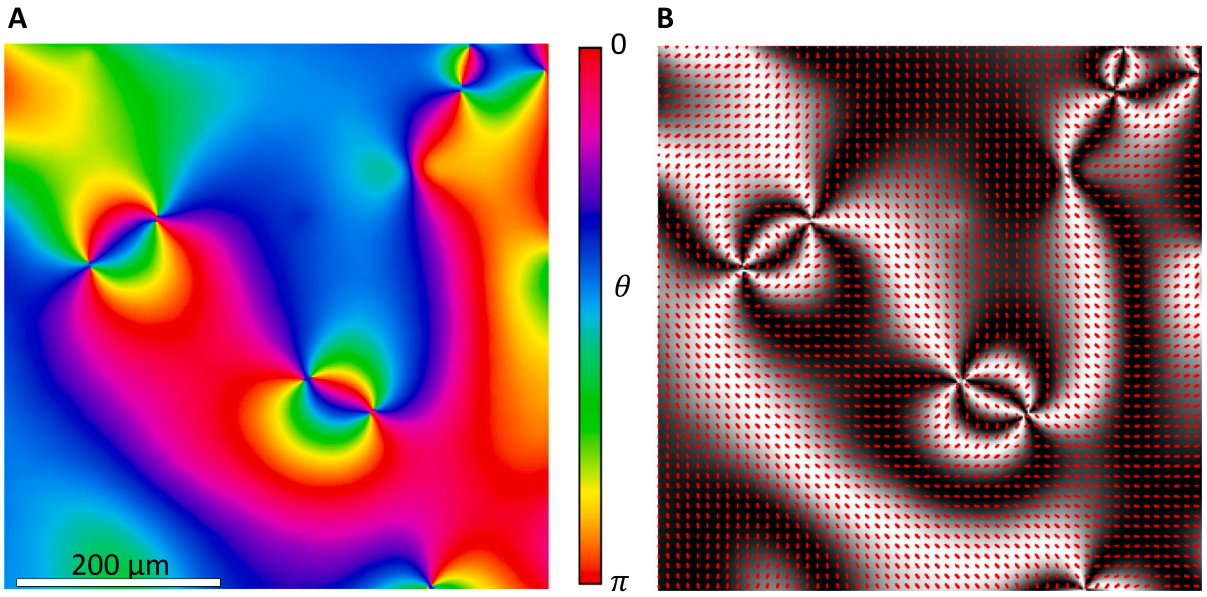

Fig. 10. Annihilation of point defects in a nematic liquid crystal. The sample is a 10 µm layer of the mixture MLC7029 from Merck. (A) Instantaneous orientational field resolved with the adaptive polarimeter. (B) Director field overlaid on the corresponding Schlieren texture between crossed polarizers, as reconstructed from the measured orientational field. See also Movie 2.

8. Validation and characterization

In the following, we will show the capabilities of this instrument by performing measurements of relevance in different areas of materials science when birefringence materials are involved. We will focus on the realtime acquisition of full polarimetry data by always studying dynamic processes in birefringent liquids, both standard liquid crystals with high birefringence, and biomaterials with very low birefringence. The signal-to-noise ratio may be improved in static scenarios, as redundant measures can be acquired and fitted to extract the orientation of the slow axis and the birefringence from data fitting. Nevertheless, we show here the performance in extreme cases, where the sensitivity and temporal response of this adaptive polarimeter stands our from current commercial implementations. Finally, we will demonstrate the simultaneous acquisition of polarimetry and fluorescence images of an active biomaterial with very low birefringence.

8.1. Characterization of defect structure and dynamics in liquid-crystalline soft materials

Liquid crystals are anisotropic fluids whose more direct signature is their birefringence [25,26]. For the simplest nematic phase (absence of long-range positional order), the lowest-energy configuration is the one where molecules are aligned over tens, even hundreds of microns. In usual applications, liquid crystals are confined as layers between parallel electrodes. Dynamic changes often lead to the formation of topological defects, or distortions of the orientational field that cannot be relaxed in a continuous way. The structure of the orientational field around these defects is usually complex, and its assessment is complicated by the ambiguity inherent to the observation between crossed polarizers. The study of defect dynamics, and its relation with surrounding material alignment is the object of fundamental interest for soft materials featuring long-range orientational order [27]. Even a precise characterization of the structures surrounding the defects is of interest to extract important materials parameters using image-based methods from systems that elude the use of traditional methods [28,29]. Moreover, the use of tailored arrays of defects of a well-known configuration in liquid crystals has the potential to build reconfigurable optical devices [30].

As a proof of concept for the temporal resolution of our instrument, we have characterized the creation and annihilation of point defects in a nematic liquid crystal layer. The liquid is confined as a layer between two transparent electrodes that force, due to chemical surface treatment, liquid crystal molecules to be oriented perpendicularly to the layer plane. By using a material whose molecules align perpendicularly to an electric field (negative dielectric anisotropy), and by applying an electric field between the two transparent electrodes, we force molecules to rotate perpendicularly to the initial configuration, leading to an energy degeneracy (all in-plane orientations will be equivalent). This leads to the formation of a large number of defects that are perceived as points under cross-polarizers (see Fig. 10).

These defects have complementary distortions (or topological charge) and they experience a mutual attraction driven to reduction of the system's elastic energy. As a result, a continuous dynamics of defect annihilation towards a defect-free state is observed. Due to the relatively high viscosity of these materials, an image rate of 1–2 Hz is usually enough to fully characterize the process, well within the capabilities of this instrument. The dynamics, as captured by the polarimeter at 2 Hz, is presented in Movie 2. Notice

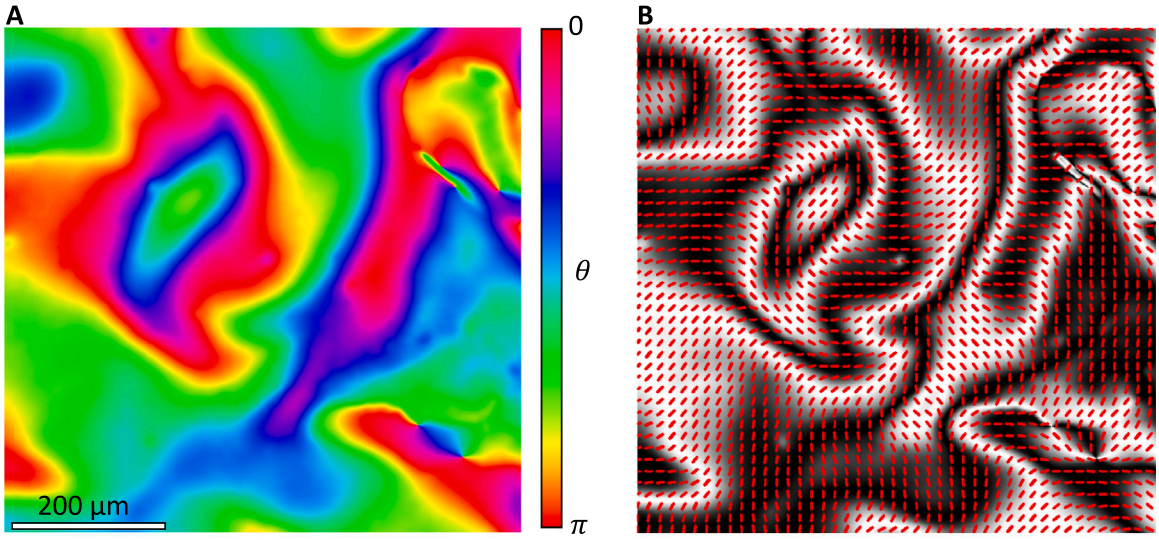

Fig. 11. Local stirring of a nematic liquid crystal. The sample is a 10 µm layer of the liquid crystal 5CB in contact with an active gel layer. (A) Instantaneous orientational field resolved with the adaptive polarimeter. (B) Director field overlaid on the corresponding Schlieren texture between crossed polarizers, as reconstructed from the measured orientational field. See also Movie 3.

that these observations would not be possible with existing commercial instruments, which lack the required temporal resolution. The raw polarimetry data for a complete analysis and alternative render is available with the uploaded material.

8.2. Characterization of soft materials under flow conditions

Many soft materials feature long-range orientational order. Besides liquid crystals, this feature is found in concentrated surfactant or lipid solutions, chromophore solutions, biomolecules, bacteria colonies, cell tissues, etc. Assessing their local order is fundamental for their study, in particular under flow conditions imposed by gradients of pressure, surface tension, external shearing, etc. In those cases, availability of a time-resolved polarimetry is of fundamental interest [31–34].

As a proof of concept, we present here an experiment where a thin layer of the nematic liquid crystal oil 5CB, often used in the literature, is put into contact with an aqueous subphase that contains an active gel of cytoskeleton proteins [35]. The continuous, turbulent-like motion of the active medium couples with the liquid crystal across the interface, resulting in complex dynamics of flow alignment and complicated patterns in the orientational field of the passive mesogen. Once more, a good temporal resolution is essential to assess this coupling across the interface, and relate the patterns imposed on the liquid crystal layer by the non-equilibrium biomaterial. In this case, a sampling rate of 1–2 Hz is perfect to capture the dynamics, well within the capabilities of our instrument, but outside the reach of existing commercial instruments, which lack the required temporal resolution.

In Fig. 11 we present a snapshot of this experiment, where we resolve the local orientational field of the mesogen. The captured dynamics is shown, in an enlarged field of view, in Movie 3. The corresponding raw polarimetry data for a complete analysis and alternative render is available with the uploaded material.

8.3. Characterization of very low birefringence materials. Simultaneous polarimetry and fluorescence

As a final example, we demonstrate the full capability of the instrument by performing the simultaneous imaging of a dynamic system using quantitative polarimetry and fluorescence. The system of choice is a kinesin/tubulin active nematic [36], formed by the in-vitro reconstitution of these cytoskeleton proteins with depletion towards an aqueous/oil interface. Typically, a fraction of the tubulin molecules are label with a fluorescence probe, which allows to visualize the self-motile, ordered filaments that constitute the system. Extraction of the local orientational field is typically performed through extensive analysis of images acquired with a high-end fluorescence camera, in a process that requires the manual-tuning of some parameters in the image processing algorithm [37], which is prone to detection errors. It is known that this biomimetic material features a small, but non-zero birefringence that can be employed to extract the local orientational field without user intervention.

As a proof of concept, we have prepared the standard fluorescent active nematic layer and demonstrate that the local orientational field extracted in real-time by our polarimeter perfectly matches the ordering of the active filaments observed in the fluorescence image. This has been performed at the usual 1–2 Hz rate that characterizes our system, about 10 times faster than similar measures reported in the literature using commercial quantitative polarimetry instruments [38]. In Fig. 12 we show a snapshot where the

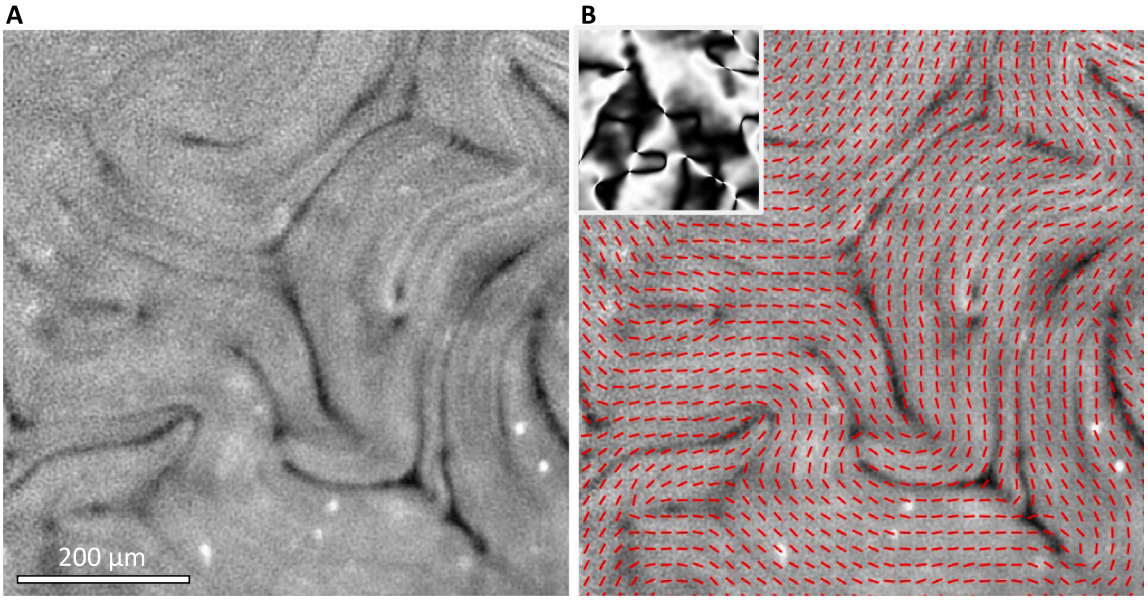

Fig. 12. Active nematic layer. The sample a layer a few microns thick of a low birefringence biomaterial made from cytoskeleton proteins. Here, some proteins are fluorescence tagged. (A) Fluorescence images obtained from the lower module of the modular microscope. (B) Fluorescence image with the director field as an overlay. The field has been extracted from the adaptive polarimeter, measured in synchrony with the fluorescence. In the inset, the Schlieren texture between crossed polarizers is computed from the orientational field. See also Movie 4.

fluorescence image is overlaid with the orientational field extracted from the polarimetry. The real time sequence can be seen in Movie 4. The corresponding raw polarimetry data for a complete analysis and alternative render is available with the uploaded material.

This system features a very small birefringence, which we estimate at 10 nm, near the limit of resolution of the instrument, but consistent with measurements reported with LC-Polscope at a much slower rate. This shows that the birefringence resolution of our microscope is comparable with existing commercial instruments, but at a much faster acquisition rate.

8.4. Capabilities and limitations

- Absolute retardance is restricted to values in the range 0 nm until 150 nm, approximately. Larger retardances have the ambiguity of an unknown multiple of the wavelength of light used. We have measured retardances as low as 10 nm at full frame rate. Even lower values should be accessible for static samples.
- Orientation of the pixel-level optical axis can be assessed for retardance values in excess of 150 nm.
- Performance of the LC retarder limits system acquisition rate to 2.5 Hz.
- Simultaneous polarimetry and fluorescence allows for more complex measurements, such as simultaneous polarimetry and particle-image velocimetry measurements, or as an alternative to multichannel/multiprobe fluorescence microscopy. However, alignment between the two optical systems must be accurately calibrated.
- The instrument is modular, which permits to implement just the quantitative polarimeter at a significantly reduced cost with respect to the dual polarimeter/fluorescence microscope. The latter capability can be easily incorporated when the need arises.
- Fluorescence intensity must be high, as the polarizing elements damp the beams in the fluorescence light path.

Declaration of competing interest

The authors declare that they have no known competing financial interests or personal relationships that could have appeared to influence the work reported in this paper.

Acknowledgments

J.I-M., F. S., and B. M. acknowledge support from MICINN/AEI/10.13039/501100011033 (Grant No. PID2019-108842GB-C22). O.A. acknowledges support from MICINN/AEI/10.13039/501100011033 (Grants No. RTI2018-098410-J-I00 and RYC2018-024997-I). B.M.-P. acknowledges funding from Generalitat de Catalunya through a FI-2018 PhD Fellowship. The authors thank Thorlabs, Inc., for allowing to reproduce the CAD designs of their optomechanical components within the graphical material of this article.

Appendix

A.1. Calibration

In this section, we explain and show the pertinent Mueller calculus we perform to calibrate all the optical devices of the polarimeter. Then, we describe how to minimize misalignments once the instrument is mounted. Before starting, we should remark that all the angles are with respect to the lab frame of reference.

A.1.1. Fast axis determination

In this section, we show the Mueller calculus involved in the alignment of polarizers and linear retarders.

A.1.1.1. Linear polarizers. → The Mueller calculus for the setup shown in Fig. 3a is given by:

$$I(\alpha) = I_0 \begin{pmatrix} 1 & 0 & 0 & 0 \end{pmatrix} \mathbf{M}(-\alpha)\mathbf{M}_{\mathrm{LHP}}\mathbf{M}(\alpha)\mathbf{M}_{\mathrm{LHP}} \begin{pmatrix} 1 \\ 0 \\ 0 \\ 0 \end{pmatrix} = \frac{I_0}{2}(\cos 2\alpha + 1) = I_0 \cos^2 \alpha \tag{15}$$

where I_0 is the light intensity coming out from the light source. Thus, the orientation with minimum light intensity is 90°. Note that Eq. (15) coincides with Malus's law.

A.1.1.2. Linear retarders (QWP and LCR). → To calibrate a LR (or linear compensator) with a fast axis oriented at α and a retardance δ, we use the setup shown in Fig. 3b, whose Mueller calculus reads:

$$I(\alpha,\delta) = I_0 \begin{pmatrix} 1 & 0 & 0 & 0 \end{pmatrix} \mathbf{M}_{\mathrm{LP}}^{90^\circ}\mathbf{M}_{\mathrm{LR}}^{-\alpha,\delta}\mathbf{M}_{\mathrm{Mirror}}\mathbf{M}_{\mathrm{LR}}^{\alpha,\delta}\mathbf{M}_{\mathrm{LHP}} \begin{pmatrix} 1 \\ 0 \\ 0 \\ 0 \end{pmatrix} = \frac{I_0}{4}\Big[(\cos 2\delta - 1)(\cos 4\alpha - 1)\Big] \tag{16}$$

where the superscripts of the Mueller matrices indicate the orientation of the fast axis of each device with respect to the lab frame reference (horizontal). Note that, with this arrangement, the beam crosses the LR from one side, hits the mirror, changes the direction, and strikes back the LR, but this time on the opposite side to the one it hit first. Consequently, if the angle of the rotation matrix of LR is the first time α, the second time, it will be $-\alpha$. This is why one of the Mueller matrices has as an orientation angle $-\alpha$.

Since the compensators we want to calibrate are QWP and the variable LCR, which can be configure to be a QWP, we can simplify Eq. (16) by substituting $\delta = \pi/2$, which is the retardance for a QWP:

$$I(\alpha) = \frac{I_0}{2}(1 - \cos 4\alpha) = \sin^2(2\alpha) \tag{17}$$

The light intensity depends on the $\cos(4\alpha)$. Thus, there is not one only minimum or maximum. The minima are at $\alpha^{\min} = 0^\circ, 90^\circ$, and the maxima $\alpha^{\max} = 45^\circ, 135^\circ$. Thus, for the calibration of these devices, we take as a first reference the fast axis provided by the manufacturer. From there, we search for the minimum or maximum light intensity, depending on the desired orientation (0° or 45°, respectively).

A.1.2. Instrument calibration

Finally, after the assembly of the setup, it is convenient to calibrate the whole assembly in order to minimize as much as possible light aberrations due to misalignments. For the sake of simplicity, we assume that the alignment errors of the QWP and the variable LCR are larger than the ones of the LHP and the LVP. Therefore, we neglect the latter ones. We also neglect the errors in the retardation of the compensators.

Let us suppose we have an optical device with a Mueller matrix $\mathbf{M}$ and with a deviation from its theoretical alignment of Δ. Then, the Mueller matrix $\mathbf{M}^{\Delta}$ that accounts for this deviation can be written as:

$$\mathbf{M}^{\Delta} = \mathbf{R}(-\Delta)\mathbf{M}\mathbf{R}(\Delta) = \begin{pmatrix} 1 & 0 & 0 & 0 \\ 0 & \cos 2\Delta & -\sin 2\Delta & 0 \\ 0 & \sin 2\Delta & \cos 2\Delta & 0 \\ 0 & 0 & 0 & 1 \end{pmatrix} \mathbf{M} \begin{pmatrix} 1 & 0 & 0 & 0 \\ 0 & \cos 2\Delta & \sin 2\Delta & 0 \\ 0 & -\sin 2\Delta & \cos 2\Delta & 0 \\ 0 & 0 & 0 & 1 \end{pmatrix} \tag{18}$$

if we consider $\Delta \to 0$, we can simplify Eq. (18) to:

$$\mathbf{M}^{\Delta} = \mathbf{R}(-\Delta)\mathbf{M}\mathbf{R}(\Delta) \approx \begin{pmatrix} 1 & 0 & 0 & 0 \\ 0 & 1 & -2\Delta & 0 \\ 0 & 2\Delta & 1 & 0 \\ 0 & 0 & 0 & 1 \end{pmatrix} \mathbf{M} \begin{pmatrix} 1 & 0 & 0 & 0 \\ 0 & 1 & 2\Delta & 0 \\ 0 & -2\Delta & 1 & 0 \\ 0 & 0 & 0 & 1 \end{pmatrix} \tag{19}$$

Note that for an optical device with a theoretical orientation of α and a deviation Δ from this angle α, we should rotate twice the Mueller matrix $\mathbf{M}$:

$$\mathbf{M}^{\alpha+\Delta} = \mathbf{R}(-\alpha)\mathbf{R}(-\Delta)\mathbf{M}\mathbf{R}(\Delta)\mathbf{R}(\alpha) \tag{20}$$

Applying Eq. (20) to the Mueller calculus of our setup without a sample and supposing that the only sources of error come from misalignments in the plQWP and the LCR:

$$\begin{aligned} I(\psi, \Delta_0, \Delta_1, \Delta_2) = \begin{pmatrix} 1 & 0 & 0 & 0 \end{pmatrix} \cdot \mathbf{M}_{\mathrm{LP}}^{90} \cdot \mathbf{M}_{\mathrm{QWP}}^{45+\Delta_2} \cdot \mathbf{M}_{\mathrm{QWP}}^{0+\Delta_1} \cdot \mathbf{M}_{\mathrm{LCR}}^{45+\Delta_0} \cdot \mathbf{M}_{\mathrm{LP}}^{0} \cdot \mathbf{S}_{\mathrm{in}} = \\ I_0[(4\Delta_0^2 + \cos\psi)(-2\Delta_2^2 + 2\Delta_1\Delta_2 + \Delta_1) + \Delta_2 \sin\psi(4\Delta_1\Delta_2 + 1) \\ - 2\Delta_0(\cos\psi - 1)(-4\Delta_1^2\Delta_2 + 4\Delta_1\Delta_2^2 + 1/2) + 1/2] \end{aligned} \tag{21}$$

where Δ_0, Δ_1 and Δ_2 are the deviations of the variable LCR, the first QWP (the one oriented at 0°), and the second QWP (the one oriented at 45°), respectively. ψ is the retardance of the variable LCR. Assuming $\Delta_0 \sim \Delta_1 \sim \Delta_2 \to 0$, we can neglect the second order terms and write a simpler form of Eq. (21):

$$I(\psi, \Delta_0, \Delta_1, \Delta_2) \approx \frac{I_0}{2}\left[(\Delta_1 - \Delta_0)\cos\psi + \Delta_2 \sin\psi + \Delta_0 + \frac{1}{2}\right] \tag{22}$$

We obtain Δ_2 by combining the light intensities at $\psi = \pi/2$ and $\psi = 3\pi/2$:

$$\Delta_2 \approx \frac{1}{2}\frac{I(\pi/2) - I(3\pi/2)}{I(\pi/2) + I(3\pi/2)} \tag{23}$$

and $(\Delta_1 - \Delta_0)$ with the light intensities at $\psi = 0$ and $\psi = \pi$:

$$(\Delta_1 - \Delta_0) \approx \frac{1}{2}\frac{I(0) - I(\pi)}{I(0) + I(\pi)} \tag{24}$$

Observe that the two deviations Δ_0 and Δ_1 cannot be isolated from each other. This is why we have to minimize them by trial and error.

References

[1] Oriol Arteaga, Marta Baldrís, Joan Antó, Adolf Canillas, Esther Pascual, Enric Bertran, Mueller matrix microscope with a dual continuous rotating compensator setup and digital demodulation, Appl. Opt. 53 (2014) 2236–2245.

[2] Ye Wang, Honghui He, Jintao Chang, Chao He, Shaoxiong Liu, Migao Li, Nan Zeng, Jian Wu, Hui Ma, Mueller matrix microscope: A quantitative tool to facilitate detections and fibrosis scorings of liver cirrhosis and cancer tissues, J. Biomed. Opt. 21 (2016) 071112.

[3] Dale Gottlieb, Oriol Arteaga, Mueller matrix imaging with a polarization camera: Application to microscopy, Opt. Express 29 (0000) 34723–34734.

[4] David C. Adams, Lida P. Hariri, Alyssa J. Miller, Yan Wang, Josalyn L. Cho, Martin Villiger, Jasmin A. Holz, Margit V. Szabari, Daniel L. Hamilos, R. Scott Harris, Jason W. Griffith, Brett E. Bouma, Andrew D. Luster, Benjamin D. Medoff, Melissa J. Suter, Birefringence microscopy platform for assessing airway smooth muscle structure and function in Vivo, Sci. Transl. Med. 8 (1–9) (2016) 359ra131.

[5] R. Oldenbourg, A new view on polarization microscopy, Nature 381 (1996) 811–812.

[6] Michael Shribak, Rudolf Oldenbourg, Techniques for fast and sensitive measurements of two-dimensional birefringence distributions, Appl. Opt. 42 (2003) 3009–3017.

[7] S.B. Mehta, M. Shribak, R. Oldenbourg, Polarized light imaging of birefringence and diattenuation at high resolution and high sensitivity, J. Opt. 15 (1–13) (2013) 094007.

[8] M. McQuilken, S.B. Mehta, A. Verma, G. Harris, R. Oldenbourg, A.S. Gladfelter. S.B. Mehta, M. Shribak, R. Oldenbourg, Polarized fluorescence microscopy to study cytoskeleton assembly and organization in live cells, Curr. Protoc. Cell Biol. 67 (1–13) (2015) 4.29.

[9] Toralf Scharf, Polarized Light in Liquid Crystals and Polymers, Wiley-Interscience, Hoboken, N.J, 2007.

[10] M.J. Shin, D.K. Yoon, Role of stimuli on liquid crystalline defects: From defect engineering to switchable functional materials, Mater. (Basel) 13 (2020).

[11] C.F. Dietrich, P.J. Collings, T. Sottmann, P. Rudquist, F. Giesselmann, Extremely small twist elastic constants in lyotropic nematic liquid crystals, Proc. Natl. Acad. Sci. U S A 117 (2020) 27238–27244.

[12] Q. Zhang, R. Zhang, B. Ge, Z. Yaqoob, P.T.C. So, I. Bischofberger, Structures and topological defects in pressure-driven lyotropic chromonic liquid crystals, Proc. Natl. Acad. Sci. U S A 118 (2021).

[13] Chenhui Peng, Oleg D. Lavrentovich, Control of micro-particles with liquid crystals, 2021, pp. 81–116.

[14] S. Das, S. Roh, N. Atzin, A. Mozaffari, X. Tang, J.J. de Pablo, N.L. Abbott, Programming solitons in liquid crystals using surface chemistry, Langmuir 38 (2022) 3575–3584.

[15] A. Opathalage, M.M. Norton, M.P.N. Juniper, B. Langeslay, S.A. Aghvami, S. Fraden, Z. Dogic, Self-organized dynamics and the transition to turbulence of confined active nematics, Proc. Natl. Acad. Sci. U S A (2019).

[16] Z. Zhou, C. Joshi, R. Liu, M.M. Norton, L. Lemma, Z. Dogic, M.F. Hagan, S. Fraden, P. Hong, Machine learning forecasting of active nematics, Soft Matter (2020).

[17] Rui-Huan Gu, Zhi-Chao Li, Jing-Wen Lang, Hua Chen, Yun Feng, Song Guo, Jing Fu, Xiao-Xi Sun, Yi-Juan Sun, Vitrification of in vitro-matured oocytes: Effects of meiotic spindle morphology on clinical outcome, Reprod. Dev. Med. 4 (2020) 18–24.

[18] M. Koike-Tani, T. Tominaga, R. Oldenbourg, T. Tani, Birefringence changes of dendrites in mouse hippocampal slices revealed with polarizing microscopy, Biophys. J. 118 (2020) 2366–2384.

[19] T. Shibahara, Y. Fukasaku, N. Miyazaki, H. Kawato, H. Minoura, Usefulness of expanding the indications of early rescue intracytoplasmic sperm injection, Reprod. Med. Biol. 21 (2022) e12432.
[20] Rachel Tkacz, Md Joynul Abedin, Phillip Sheath, Shalin B. Mehta, Amitabh Verma, Rudolf Oldenbourg, Mainak Majumder, Phase transition and liquid crystalline organization of colloidal graphene oxide as a function of ph, Particle Particle Syst. Character. 34 (2017).
[21] Kaili Hu, Yanhui Huang, Benhua Fei, Chunli Yao, Chang Zhao, Investigation of the multilayered structure and microfibril angle of different types of bamboo cell walls at the micro/nano level using a lc-polscope imaging system, Cellulose 24 (2017) 4611–4625.
[22] B. Diederich, R. Lachmann, S. Carlstedt, B. Marsikova, H. Wang, X. Uwurukundo, A.S. Mosig, R. Heintzmann, A versatile and customizable low-cost 3d-printed open standard for microscopic imaging, Nature Commun. 11 (2020) 5979.
[23] J. Hohlbein, B. Diederich, B. Marsikova, E.G. Reynaud, S. Holden, W. Jahr, R. Haase, K. Prakash, Open microscopy in the life sciences: Quo vadis? Nature Methods 19 (2022) 1020–1025.
[24] Xiaoyan Cui, Shane M. Nichols, Oriol Arteaga, John Freudenthal, Froilanny Paula, Alexander G. Shtukenberg, Bart Kahr, Dichroism in helicoidal crystals, J. Am. Chem. Soc. 138 (2016) 12211–12218.
[25] Ian W. Hamley, Introduction to Soft Matter - Revised Edition : Synthetic and Biological Self-Assembling Materials, Wiley, John Wiley [distributor], Chichester, Hoboken, N.J., 2007, rev. ed. edition.
[26] Patrick Oswald, Pawel Pieranski, Nematic and cholesteric liquid crystals : Concepts and physical properties illustrated by experiments, in: The liquid crystals book series, Taylor & Francis, Boca Raton, 2005.
[27] C. Blanch-Mercader, P. Guillamat, A. Roux, K. Kruse, Quantifying material properties of cell monolayers by analyzing integer topological defects, Phys. Rev. Lett. 126 (2021) 028101.
[28] S. Zhou, S.V. Shiyanovskii, H.S. Park, O.D. Lavrentovich, Fine structure of the topological defect cores studied for disclinations in lyotropic chromonic liquid crystals, Nature Commun. 8 (2017) 14974.
[29] N. Kumar, R. Zhang, J.J. de Pablo, M.L. Gardel, Tunable structure and dynamics of active liquid crystals, Sci. Adv. 4 (2018) eaat7779.
[30] G. Park, A. Suh, H. Zhao, C. Lee, Y.S. Choi, II. Smalyukh, D.K. Yoon, Fabrication of arrays of topological solitons in patterned chiral liquid crystals for real-time observation of morphogenesis, Adv. Mater. 34 (2022) e2201749.
[31] S. Zhou, A. Sokolov, O.D. Lavrentovich, I.S. Aranson, Living liquid crystals, Proc. Natl. Acad. Sci. USA 111 (2014) 1265–1270.
[32] L. Giomi, Z. Kos, M. Ravnik, A. Sengupta, Cross-talk between topological defects in different fields revealed by nematic microfluidics, Proc. Natl. Acad. Sci. U S A (2017).
[33] C. Blanch-Mercader, V. Yashunsky, S. Garcia, G. Duclos, L. Giomi, P. Silberzan, Turbulent dynamics of epithelial cell cultures, Phys. Rev. Lett. 120 (2018) 208101.
[34] Anupam Sengupta, Microbial active matter: A topological framework, Front. Phys. 8 (2020).
[35] T. Sanchez, D.T. Chen, S.J. DeCamp, M. Heymann, Z. Dogic, Spontaneous motion in hierarchically assembled active matter, Nature 491 (2012) 431–434.
[36] A. Doostmohammadi, J. Ignes-Mullol, J.M. Yeomans, F. Sagues, Active nematics, Nature Commun. 9 (2018) 3246.
[37] Perry W. Ellis, Daniel J.G. Pearce, Ya-Wen Chang, Guillermo Goldsztein, Luca Giomi, Alberto Fernandez-Nieves, Curvature-induced defect unbinding and dynamics in active nematic toroids, Nat. Phys. 14 (2017) 85–90.
[38] Stephen J. DeCamp, Gabriel S. Redner, Aparna Baskaran, Michael F. Hagan, Zvonimir Dogic, Orientational order of motile defects in active nematics, Nat. Mater. 14 (2015) 1110–1115.

Jordi Ignés-Mullol is an assistant professor of Physical Chemistry at the University of Barcelona. He holds a Ph.D. in experimental Soft Matter Physics (University of Pittsburgh) and was a postdoctoral fellow at Ecole Normale Supérieure de Lyon and at Tulane University. He leads an experimental soft matter laboratory that studies a wide range of materials, such as colloidal suspensions and assemblies, liquid crystals, Langmuir–Blodgett films, and biomaterials, often combining two of more of such systems.